DISCLAIMER

Final Technical Report for the DOE Award No. DE-SC0016945

Title: **New Deformation Mechanisms in Nanocrystalline Nano-porous Small Scale Metals as Defined by Kinetically-driven Microstructures**

PI: Julia R Greer (Caltech)

This supplement was to support the final research activities within the PI's former DOE BES grant focused on fundamental investigations into the link between mechanical properties and atomic-level microstructure of additively manufactured nanocrystalline metals. The hydrogel infusion additive manufacturing (HIAM) fabrication technique with hydrothermal oxidation and reduction steps developed by PI Greer group, coupled with nanomechanical experiments and simulations, demonstrate that *micro-sized* Cu and CuNi alloys produced via HIAM contain high densities of special boundaries, including coherent twin, Σ3 and other CSL boundaries, and exhibit ~ 0.4-0.6 GPa greater hardness compared with literature. The results from existing BES grant demonstrate that twin boundaries and solid solution hardening alone do not explain an uncharacteristically high hardness measured in HIAM micro-sized Cu, Ni, and cupronickel alloys. The 1.5x relative increase in the adjusted hardness of pure metals as compared to alloys hints at *a greater material-, microstructure-, and size-dependent relationship to these plasticity processes than seen in other manufacturing methods*. Another key finding from existing BES grant is that when the dimensions of HIAM Ni are reduced to nanoscale, the microstructure becomes even more complex: nanocrystalline and nano-porous, with a single grain spanning each ligand, that is contained within an individual nano-pillar. Most recent findings indicate that the yield strength of these nanocrystalline and nano-porous nano-pillars, with diameters between 160 and 300nm, is ~2x higher than those in reported nanocrystalline Ni nano- and micro-pillar compressions.

Thrust 1: The complex emergent microstructure and ensuing enhanced mechanical response of HIAM-produced Ni and Cu, as well as of their alloys with micro- and nano-scale dimensions opens a new avenue for investigating complex material behavior. It implies the existence of *new deformation mechanisms that drive the strength enhancement in kinetically driven microstructures in metals*. The broad range of interesting and unusual microstructures that can be accessed via simultaneous solid-state kinetic processes of oxide-to-metal reduction, sintering, grain growth, and boundary formation during HIAM, calls for an in-depth investigation of new deformation mechanisms available in these materials systems.

We hypothesized that the rich microstructural energy landscape within micron- and nano-sized pure metals and alloys, formed via infusion of metal salts into hydrogel templates in liquid state followed by two-step hydrothermal oxidation and reduction, incites new mechanical deformation mechanisms. The new mechanisms are expected to emerge upon deformation because of the spatially inhomogeneous distribution of surface relaxation sites (i.e. nano-pores) and plasticity-carrying constituents (i.e. nanocrystalline ligands), as well as particular energetics of kinetically formed grain and twin boundaries. The mechanical properties, i.e. yield strength, deformability, and tensile response, of micro- and nano-sized additively manufactured, nanocrystalline and nano-porous metals (Ni, Cu, and their alloys) are defined by the synergy between inhomogeneously distributed ligands with one or more grains that subtend their diameter and the combination of adjacent free volume and the non-equilibrium energetics of dominant grain boundaries.

Thrust 2: Hydrogel infusion-based additive manufacturing (HIAM) enables the 3D printing of microscale alloys through serial thermal treatments of metal ion infused gels that grow

nanocrystalline oxides and subsequently transform them into metallic phases. While a chemically versatile technique, little is understood about the multiscale microstructural impact of HIAM's unique pathways for solid-state processing. Through an in-depth characterization of HIAM-fabricated Cu_xNi alloys via electron backscatter diffraction (EBSD), transmission electron microscopy (TEM), nanoindentation, and site-specific micropillar compression, we elucidate the multiscale microstructural features and structural properties of HIAM alloys. Substantial grain growth drives the formation of annealing twins while TEM analysis uncovers nanoscale hierarchical metal-oxide structures stemming from incomplete reduction. These features elevate average nanoindentation hardnesses to a constant ~2 GPa regardless of composition. However, site-specific micropillar compressions show weakening in Cu-rich pillars and suppression of the extrinsic size effect in near-equiatomic pillars, revealing a compositional dependence of lattice and nano-scale mechanical mechanisms. This work highlights the multiscale nature of HIAM alloys and uncovers key insights for future microstructural engineering in additively manufactured alloys.

The specific research tasks in this proposal included: **(1)** Identifying parameter space to elicit specific microstructural features, i.e. nano-crystallinity (grain size), nano-porisity (pore size), and number of grains per ligand using HIAM and TEM/EBSD; **(2)** Determining the energetics of kinetically formed grain boundaries and ligand size/gain distribution via nanomechanical experiments and molecular dynamics (MD) simulations; and **(3)** Uncovering new deformation mechanisms available to microstructures with dominant characteristics, for example ligands that subtend a single grain vs. multiple ones, the free volume-enabled surface relaxation in the sample interior, and the presence of a dominant grain boundary.

Successful execution of this work would help uncover new deformation mechanisms that emerge in small-scale metallic samples, produced via additive manufacturing, as a result of their kinetically-driven microstructures that contain inhomogeneously distributed nano-sized grains and pores, ligands, and may have unusual grain and twin boundary characteristics/energetics.

Supported personnel: Dr. Wenxin Zhang and research of Dr. Thomas Tran (both defended their Ph.D. dissertations in 2025)

Publications:

1. Zhang, W., Li, Z., Dang, R., Tran, T.T., Gallivan, R.A., Gao, H., Greer, J.R. "Suppressed Size Effect in Nanopillars with Hierarchical Microstructures Enabled by Nanoscale Additive Manufacturing." ***Nano Letters*** 23(17) 8162. (2023) DOI: 10.1021/acs.nanolett.3c02309.
2. Zhang, W., Li, Z., Gao, H., Greer, J.R. "Hydrogel-Infusion-Based Additive Manufacturing of Nano-Architected Metals – Exploring the Nanoporosity-Driven Deformation Regime." ***Nature Comms*** (in review, 2025)
3. Thomas T. Tran, Rebecca A. Gallivan, and Julia R. Greer "Multiscale Microstructural and Mechanical Characterization of Cu-Ni Binary Alloys Reduced During Hydrogel Infusion Additive Manufacturing (HIAM)" ***Small*** (in revision, 2025)

Honors/Awards during Performance Period:

Julia R Greer, PI

2025 Elected member of the **National Academy of Sciences**

2024 **A.C. Eringen Medal** (SES meeting), **ASME Nadai Medal**, **Koiter lecturer** (NetherlandSchool of Mechanics), **Samuel M. McElvain** Academic Lecturer in Materials Chemistry (UW Madison), **Warren Lecture** (U Minnesota)

2023 **Fellow** of Int'l Association Adv Materials (IAAM), ***Thayer Visionaries in Technology*** Distinguished Speaker (Dartmouth), ***David Pope*** Distinguished Lecture (UPenn)

Wenxin Zhang, supported PhD student: Selected for ME Rising Stars workshop at UC Berkeley (by invitation-only), presented results supported by the DOE at the annual TMS conferences (2024, 2025) and the focused Gordon Research Conferences (GRC, 2024)

Thomas Tran, PhD student whose research was supported by this grant: Presented results at the annual TMS conferences (2024, 2025) and the nanomechanics-focused Gordon Research Conferences (GRC, 2024).

Final Technical Summary.

This report describes recent advances in the design and fabrication of nanostructured metallic pillars with hierarchical microstructures using a novel nanoscale additive manufacturing approach. Through a hydrogel-infusion-based two-photon lithography (TPL) method, we successfully fabricated 3D nickel nanopillars exhibiting both nanocrystalline and nanoporous features. The resulting "bamboo-like" internal architecture comprises 30–50 nm grains and voids with similarly scaled pores. These geometrically tunable pillars, with diameters ranging from ~130 to 550 nm, serve as an ideal platform for probing deformation mechanisms in structurally heterogeneous metals at the nanoscale.

Methods

We prepared customized photoresists for two photon lithography (TPL) to produce samples with pre designed geometries. The two-photon initiator 7-diethylamino-3-thenolcoumarin (DETC, Exciton) was dissolved in dimethyl sulfoxide (DMSO, Sigma-Aldrich) at 1-mg DETC per 75-μL DMSO. The solution was mixed with poly(ethylene glycol) diacrylate Mn = 575 (PEGda 575, Sigma-Aldrich) and deionized water at a volumetric ratio of 1:7.3:2.7, forming a yellow solution as the finished photoresist. TPL printing was performed on Photonic Professional GT (Nanoscribe GmbH) with a Zeiss Plan-Apochromat 63x/1.4 Oil DIC objective at a laser power of 50 mW and speed of 1.5 mm/s. Pillars (diameter = 2 μm; aspect ratio = 3) on top of a 3 μm-tall one-layer square lattice support were printed on Si wafers. The printed samples were then developed in deionized water for 5 minutes to form the blank hydrogel templates and subsequently submerged into a 0.002–1M aqueous solution of nickel nitrate hexahydrate (99.999%, Sigma-Aldrich) at 40°C for 60 minutes (Figure 3.2B) to form a Ni-infused hydrogel.

Then, the samples were moved from the solution to the tube furnace (MTI OTF-1500X) for two-step thermal treatment: (i) open-to-air calcination by heating at 1°C/min to 500 °C and cooling at 3°C/min back to the room temperature (Figure 3.2C); (ii) reduction by heating at 3°C/min to 590°C under vacuum, holding at 590°C for 3 min under 100-Torr forming gas (FG; 95% N2 and 5% H2), and cooling at 3°C/min back to the room temperature under vacuum. The final product was temporarily stored in Ar environment before transferred to high-vacuum conditions for further characterizations.

Research

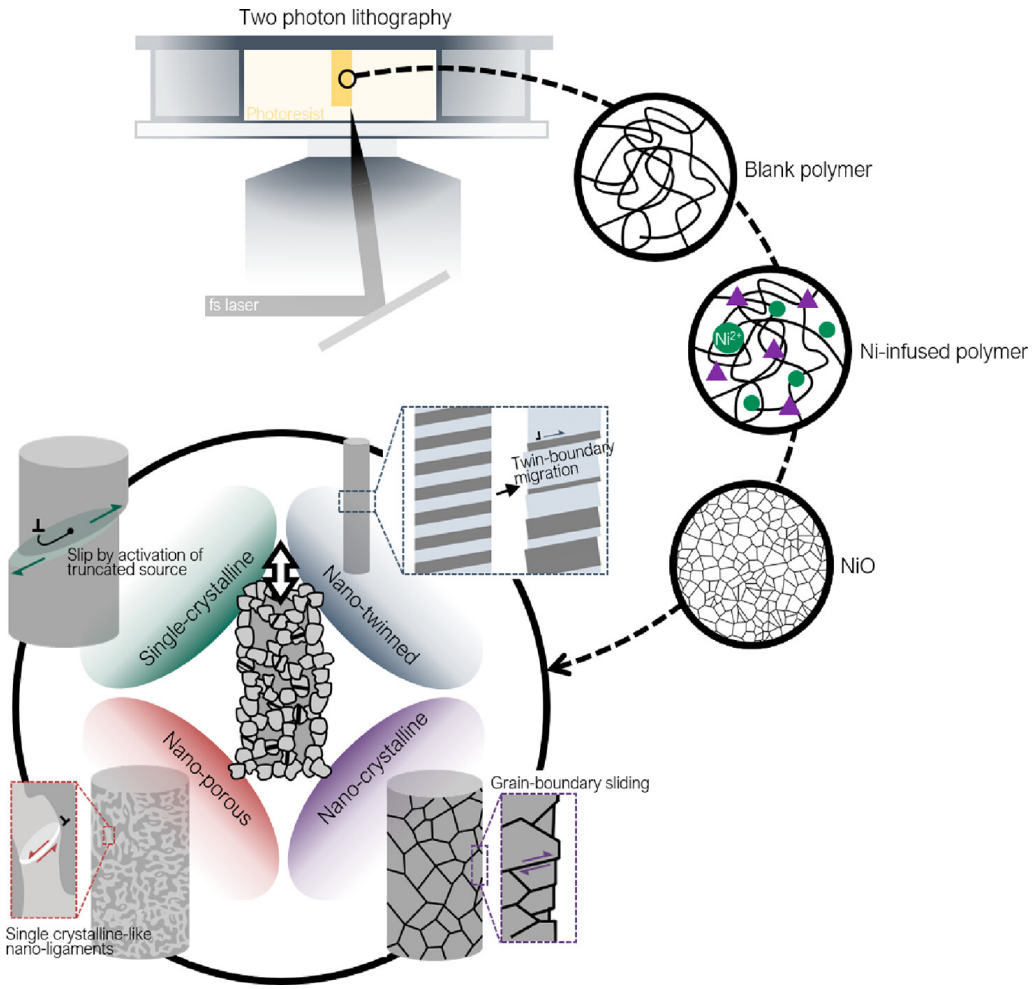

Figure 1. Additive manufacturing enables hierarchical microstructures at the nanopillar level. The multistep, two-photon-lithography-based additive manufacturing method, forming intermediate products of blank polymer, Ni-infused polymer, and NiO along the way, enables the fabrication of Ni nanopillars with hierarchical microstructures. The complex microstructure leads to interplay between the signature plasticity mechanisms of individual microstructural characteristics (i.e., single-crystallinity, nanoporosity, nanocrystallinity, and nanotwinning).

Accomplishments

The fabricated nanopillars were characterized using high-resolution transmission and scanning electron microscopy, revealing the presence of equiaxed nanograins and ligament-pore networks within each structure. In situ uniaxial compression experiments demonstrated exceptionally high strengths (1–3 GPa) and, more importantly, a significantly **suppressed size effect**, with flow stress scaling as $\sigma \propto D^{-0.2}$ — much lower than typical scaling in defect-free single-crystalline pillars. Deformation mode analysis revealed a size-dependent transition: smaller pillars exhibited localized shear banding, while larger ones underwent more distributed plastic deformation. These results challenge the classical view that porosity and internal heterogeneity weaken nanostructures

Individual pillars experienced significant volumetric shrinkage, primarily during the air-calcination step and secondarily during the forming gas reduction step, while maintaining their shape integrity. Pillars printed with the prescribed diameter of 2 μm at the TPL step resulted in the final diameter, D, of ~130–550 nm and an aspect ratio of ~3-4. The crystallographic structure of the intermediate (post-calcination, NiO) and final (post-reduction, Ni) products was characterized via high resolution TEM (HR-TEM) and indexed based on the corresponding FFTs.

Post-calcination. The intermediate product was determined as a cubic-phase NiO with a lattice parameter of 4.17 Å and Fm3m symmetry and contained uniformly distributed ~5– 10 nm-sized grains (Figure 3.6). These oxide pillars were mostly fully dense for diameters, $D \lesssim 350$ nm; larger pillars inevitably contained an artifact void (Figure 3.6), which was continuous in the longitudinal direction, dividing the NiO pillar into a solid core and a shell.

Post-reduction. The final product was determined to be fcc Ni with a lattice parameter of 3.52 Å, with a grain size, d, ~30–50 nm, and finite porosity. All Ni pillars with $D \lesssim 300$ nm were ~10% porous when reduced from fully dense NiO intermediate product. The vertical-cut cross-sectional lamella, shown in Figure 3.6, demonstrates that these smaller pillars were typically comprised of a continuous exterior wall, as well as interior ligaments and pores. TEM image of a representative wall segment, shown in Figure 3.6, uncovers a bamboo-like microstructure, with individual nano-grain d ~ 30–50 nm, subtending the walls and ligaments, which are thus 1–2 grain-wide. The pores, which have critical dimensions comparable to d, are stochastically distributed throughout the sample, independent of pillar size, meaning that a larger pillar would on average have more ligaments than a smaller pillar, rather than being self-similarly scaled up. The labeled Si(Ox) in Figure 3.6C(i–ii) correspond to the TEM lift-out artifacts resulting from FIB-milled substrate Si re-deposition and oxidation.

We found that the larger pillars with $D > 300$–350 nm had greater porosity, which increased from 10% for D ~ 300 nm to ~20–25% for D ~ 550 nm, and contained large, longitudinal core-shell voids retained through the FG-reduction. As-calcined NiO intermediate product is fully dense at smaller D but forming such longitudinal porosity defect at larger D,which is retained through reduction.

Considering the microstructural inhomogeneity in the larger pillars, we gravitate our mechanical characterization and discussion (*in situ* nano-compression and MD simulations) on smaller pillars with $D \lesssim 350$ nm, which are free of the core-shell voids.

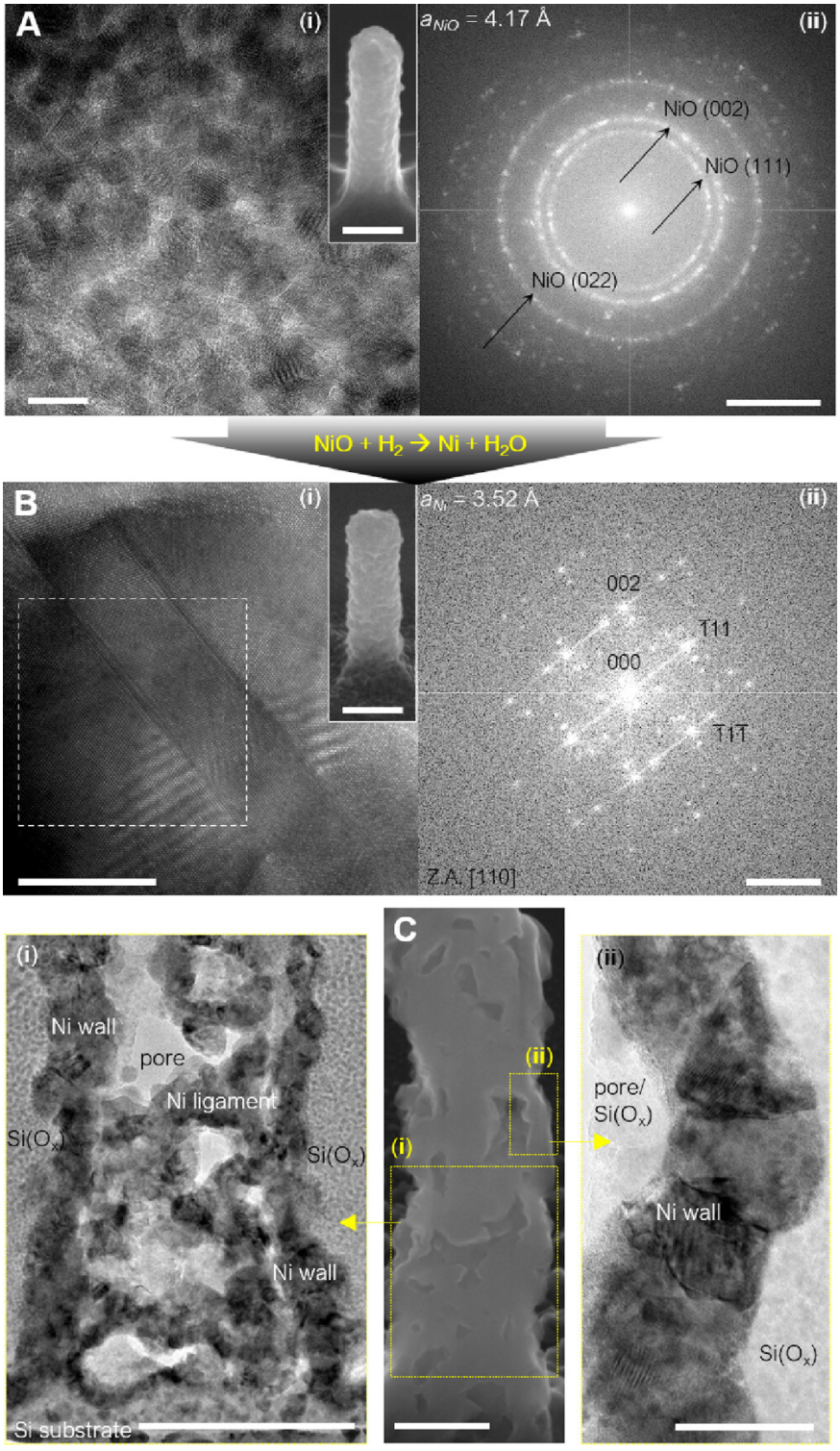

Figure 3.6 Microstructural characterization of fabrication products. (**A**) (i): HR-TEM micrographs (scalebar = 10 nm) of a representative NiO lamella FIB-carved from a nanopillar; (i-Inset): SEM micrographs of a typical NiO nanopillar (scalebar = 250 nm); (ii) fast Fourier transformation (scalebar = 5 nm^{-1}) of the image area in A(i). (**B**) (i): HR-TEM micrographs (scalebar = 10 nm) of a representative reduced Ni lamella; (i-Inset): SEM micrographs of a typical Ni nanopillar (scalebar = 250 nm); (ii) fast Fourier transformation (scalebar = 5 nm^{-1}) of the dash-boxed area in B(i). (**C**) Center, SEM micrograph (scalebar = 200 nm) of a FIB-cut vertical cross-section of a typical Ni nanopillar; (i-ii) TEM micrographs of areas similar to the boxed areas displaying wall-ligament-pore microstructural features (scalebar = 200 nm and 50 nm, respectively). The redeposited $Si(O_x)$ areas in (C(ii)) are shaded for clearer view.

Size-dependence of nanopillar yield strengths. Based on compression results from $N = 56$ smaller nanopillars and $N = 44$ larger nanopillars, we observed two distinct "smaller is stronger" size-dependent regimes of their uniaxial yield strength, σ, plotted as a function of D on a log-log scale in Figure 3.10, accompanied by yield strength values from previous literatures on conventionally manufactured Ni nanopillars and nanocrystals with single- crystalline (sc), nanocrystalline (nc) microstructures. Our experiments revealed σ-D scaling following:

$$\sigma \propto D^{-\frac{dim}{m}} = D^{-\beta}$$

where $\beta = dim/m$ relates the scaling factor, β, to Weibull modulus, m, and dimensionality, dim (e.g., $dim = 2$ for surface-mediated plasticity) Smaller β, i.e., greater m at fixed dim, implies the presence of fewer and/or less severe defects in the Weibull distribution-characterized defect dominated material strength model. A clear two-regime size effect is observed, where a segment wise least-square fitting provides a value of $\beta \sim 0.2$ on $D \lesssim 350$nm, representing a suppressed extrinsic size effect for the smaller Ni nanopillars and a value of $\beta \sim 4$ on $D \gtrsim 350$ nm, representing an escalated extrinsic size effect for the larger Ni nanopillars. This significantly greater scaling factor of the latter indicates the presence of more defects or increasingly more severe defects with increasing D, agreeing with the positive correlation between porosity and D measured from pillar cross-sections.

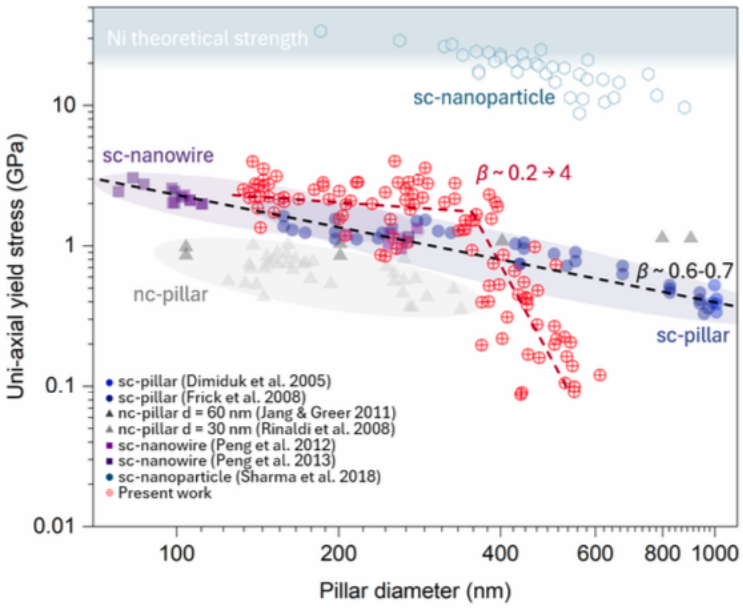

Figure 3.10 Extrinsic size effects in Ni nanomechanics[83,108–110,139–141]**.** A log-log plot of compressive uniaxial yield strengths of individual micro/nanosized Ni samples as a function of diameter. Shaded domains and dashed trend lines are used for eye guidance.

Computational Insights

To understand the origins of this mechanical robustness, the team conducted atomistic simulations using molecular dynamics. Simulations reproduced the experimentally observed strength trends and clarified the underlying deformation mechanisms. Specifically, stress relaxation occurred via a combination of surface grain boundary sliding and dislocation activity nucleating from the intersections of internal pores and grain boundaries. This dual-mode deformation pathway

provides a mechanism for distributing plasticity while suppressing catastrophic failure, which is typically a limiting factor in small-scale materials.

Broader Impacts and Applications

This work represents a substantial contribution to the fundamental understanding of size effects in heterogeneous nanostructured metals and introduces a versatile platform for creating mechanically resilient micro-architected materials. The process was demonstrated to be generalizable, with examples fabricated in Ni, Fe_2O_3, and Ag, including complex geometries like gyroids and shell-based lattices. These results have important implications for the development of next-generation microscale devices in fields such as flexible electronics, microelectromechanical systems (MEMS), biomedical microtools, and energy harvesting devices, where strength, resilience, and miniaturization must coexist.

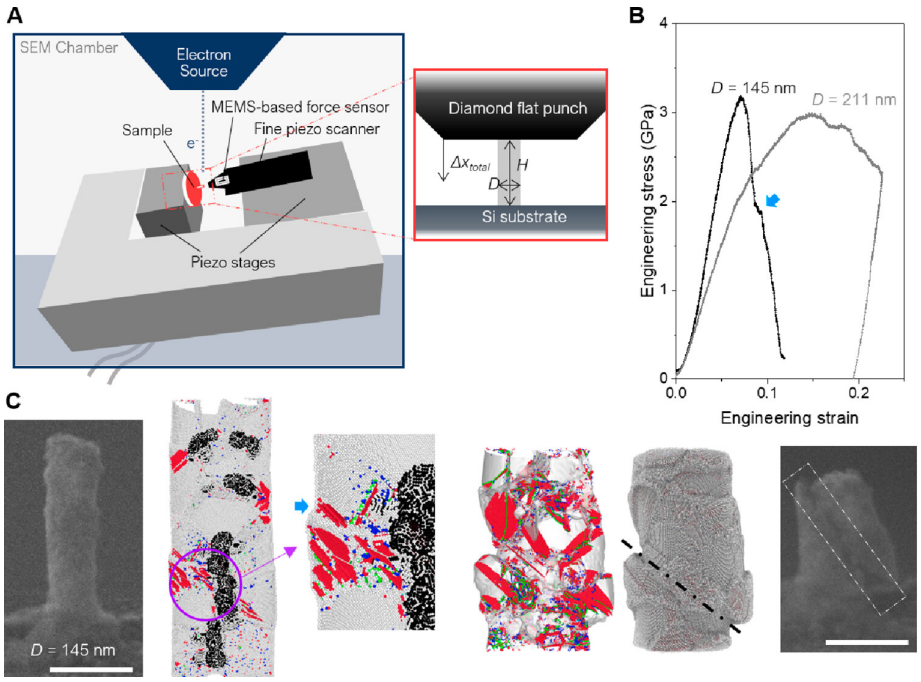

Figure 3.11 Molecular dynamics simulation of Ni nanopillars compression. (i) SEM micrographs of the original nanopillars in the suppressed size effect regime shown in Figure 3.9 labeled with a corresponding *D*, MD-simulated visualization of a representative nanopillar (ii) shortly after yielding, $e = 0.025$, and (iii) at a significant plastic strain, $e = 0.3$, and (iv) post-mortem SEM micrographs of the same pillars (all scalebars = 250 nm). Dislocations are colored by their types: Shockley partial dislocations (green), stair-rod dislocations (pink), and Hirth dislocations (yellow); atoms with hcp, bcc, and unknown coordination are colored red, blue, and white, respectively; in MD visualization, bulk fcc atoms are removed for clearer view; in (ii), atoms on the internal void surface are colored black, and blue arrows indicate the surface steps formed by grain boundary sliding.

In the PI's group's earlier work, Saccone & Gallivan et. al reported considerably high twin densities for HIAM-fabricated Cu and $Cu_{50}Ni_{50}$, which partly contributed to their high nanoindentation hardnesses exceeding literature values by 47% and 15%, respectively (.

Additional anomalous hardening was hypothesized to result from the unique processing conditions of HIAM. The extent of this hardening will be further explored in the present study in the context of HIAM's microstructural evolution. In this work, we use HIAM to synthesize alloys across the Cu_xNi compositional range to investigate what defects and mechanical properties arise in metals and alloys fabricated by the reductive annealing process. We investigate how alloy composition impacts microstructural evolution based on the proportions and types of pre-existing oxide phases present prior to the reductive annealing treatment. Electron back scatter diffraction (EBSD) and transmission electron microscopy (TEM) techniques examine the specific microstructural features in HIAM alloys that result from their complex thermal history and phase evolution. Single crystal micropillar compressions in addition to nanoindentation hardness measurements probe the strengthening mechanisms due to lattice or nanoscale defects without the contributions of interfaces and macroscale features. By investigating the process-structure-property relationship of HIAM alloys across multiple length scales, we aim to further develop a mechanistic understanding of HIAM's phase evolution and corresponding strengthening mechanisms as a function of composition, as well as provide insights into how the process can be used to engineer AM microstructures inaccessible by current metal AM technology.

Fig. 1 shows the fabrication route for producing Cu_xNi alloys via HIAM and depicts the typical morphology of Cu_xNi honeycomb structures after calcining (**Fig. 1a**) and subsequent reduction in forming gas (N_2-5% H_2 mixture) **(Fig. 1b)**. Print geometry is maintained throughout the thermal treatments (**Fig. 1b(i)** and **Fig. 1c(i)**). Upon calcining, the gel structure is converted to a highly porous nanocrystalline mixture of CuO and NiO phases **(Fig. 1b(ii))**. Following a subsequent reductive annealing process, the surface morphology of all Cu_xNi alloys resembles a well-annealed polycrystal with prominent crystal facets and twin boundaries **(Fig. 1c(ii), Fig. 2).** Some observed defects include aluminosilicate inclusions and sparsely distributed internal porosity. These defects are consistent with the reported defects in HIAM-synthesized pure Cu and Ni **[11]**. Alloy chemistry does not impact the presence of aluminosilicate inclusions **(Supp. Fig. 2)**.

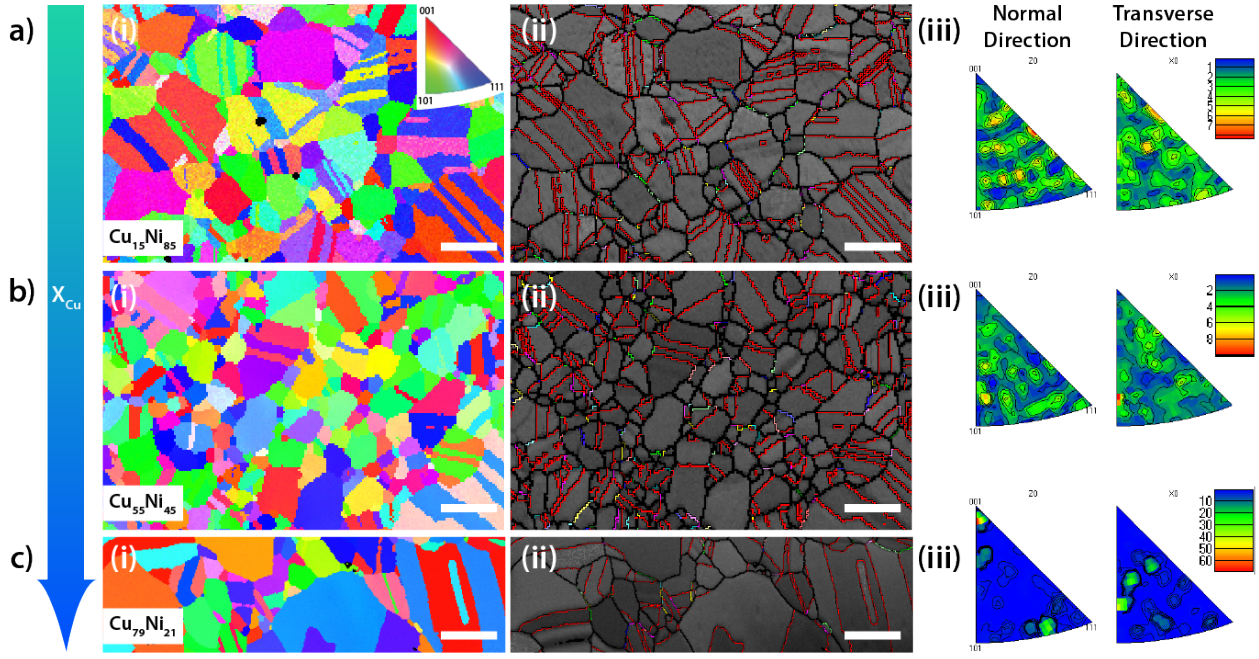

Figure 2. EBSD analysis of HIAM Cu_xNi alloys. (a, b, c) (i) Orientation maps of $Cu_{15}Ni_{85}$, $Cu_{55}Ni_{45}$, and $Cu_{79}Ni_{21}$. Coloring is based on the specimen z-axis inverse pole figure coloring according to the stereographic triangle (scale bar 5 μm). **(a, b, c) (ii)** Boundary maps show profuse annealing twinning, with high angle grain boundaries (misorientation > 10°) outlined in black and

Σ3 twins in red over a Kikuchi band contrast image. Higher order CSL boundaries are demarcated by other colors, including green for Σ5, blue for Σ7, and pink for Σ9 (scale bar 5 μm). **(a, b, c) (iii)** Inverse pole figures of specimen normal and transverse directions demonstrate the random orientation of HIAM Cu_xNi.

Fig. 2 highlights the equiaxed and randomly oriented grain morphologies of various Cu_xNi alloys through EBSD mapping of polished sections. This microstructure holds for both axial and transverse cross-sections of the honeycomb lattices. EBSD could only index one phase in the HIAM Cu_xNi alloys: the FCC solid solution of Cu and Ni **(Supp. Fig. 3)**. Grain size analysis shows an average grain size and standard error of 2.6 ± 0.19 μm for 15% Cu ($Cu_{15}Ni_{85}$), 2.3 ± 0.04 μm for 55% Cu ($Cu_{55}Ni_{45}$), and 4.3 ± 0.48 μm for nominally 80% Cu ($Cu_{79}Ni_{21}$). The grain sizes follow a lognormal distribution with all alloys containing some large grains in excess of 30 μm. **Fig. 2a(ii), 2b(ii),** and **3b(ii)** depicts the high twin boundary density present across all representative alloys. Twin boundaries are indicated by red lines while other higher order coincident site lattice (CSL) boundaries are marked by blue, pink, yellow, and green lines. Twin boundaries alone make up 50.6% of all boundaries in $Cu_{15}Ni_{85}$ with a line density of 0.85 μm^{-1}, with similar values for other HIAM CuNi, Cu, and Ni.

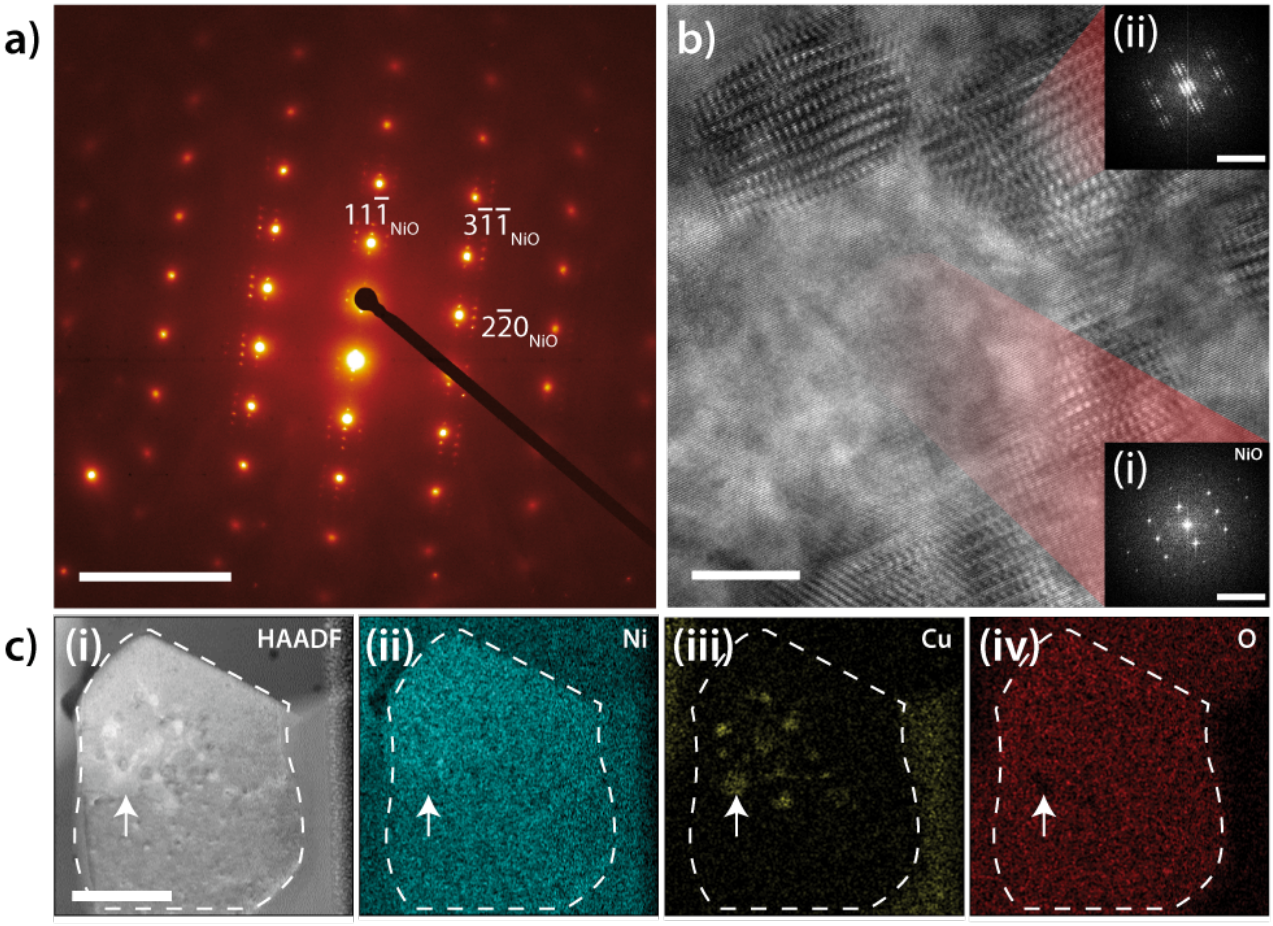

Figure 3. Double-diffracting hierarchical metal-oxide structure in $Cu_{17}Ni_{83}$. (a) SADP depicting double diffraction of FCC Ni and NiO crystals along their <112> zone axis (scale bar 10 nm^{-1}). **(b)** HRTEM and FFT diffractograms of the selected area indicate multiple nanoinclusions in a NiO matrix (HRTEM scale bar 10 nm, FFT scale bar 10 nm^{-1}) which are identified as brighter Z-contrast in **(c)(i)** STEM-HAADF and as increased counts of Cu and decreased counts of oxygen in **(c)(ii-iv)** STEM-EDS (scale bar 200 nm).

Fig. 3 illuminates additional nanostructural features in a representative $Cu_{17}Ni_{83}$ alloy lamella. Isolated nanovoids with sub-50 nm diameters exist within grain interiors, and larger pores

on the order of 100s of nm exist alongside grain boundaries and grains which appear darker in STEM high-angle annular dark field (HAADF) images **(Fig. 3c(i), Supp. Fig. 4)**. Z-contrast also reveals bright nano-inclusions within the darker contrast grains **(Supp. Fig 4b).** Selected area diffraction patterns (SADP) of these grains exhibit strong double diffraction effects **(Fig. 3a)**. The more intense fundamental reflections are indexed and belong to the <112>-oriented FCC rock salt crystal structure of NiO (a = 4.2 Å). The satellite reflections arise due to epitaxially oriented FCC Cu_xNi (a = 3.5-3.6 Å based on composition) (i.e., $<112>_{NiO} \parallel <112>_{CuNi}$), where the diffracted intensities from NiO are doubly diffracted through the smaller Cu_xNi lattice (i.e., the numerous satellites arise due to the Cu_xNi spot pattern being duplicated at every NiO diffraction spot). HRTEM images further substantiate that these inclusions are Cu_xNi nuclei since the periodicity of the translational Moiré fringing is commensurate with parallel, overlapping FCC Cu_xNi and NiO planes **(Fig. 3b)**. Fast Fourier Transforms (FFT) indicates lattice spacing of the matrix phase matches that of NiO **(Fig. 3b(i))**, and the same analysis on Moiré fringed areas provides diffractograms replicating the double diffraction effects observed in SADP **(Fig. 3b(ii))**. STEM-EDS mapping also indicates a heterogeneous distribution of Cu and O content between grains representative of the observed Cu_xNi-NiO structure **(Fig. 3cii-iv).** Besides the metallic nuclei within oxide grains, the oxide phase is also identified in other orientation relationships. Adjacent alloy grains in $Cu_{17}Ni_{83}$ contain smaller epitaxial NiO inclusions **(Supp. Fig. 7)**, and $Cu_{56}Ni_{44}$ contains similar sized but incoherent NiO in the CuNi matrix, depicted by diffraction rings in its SADP **(Supp. Fig. 8).**

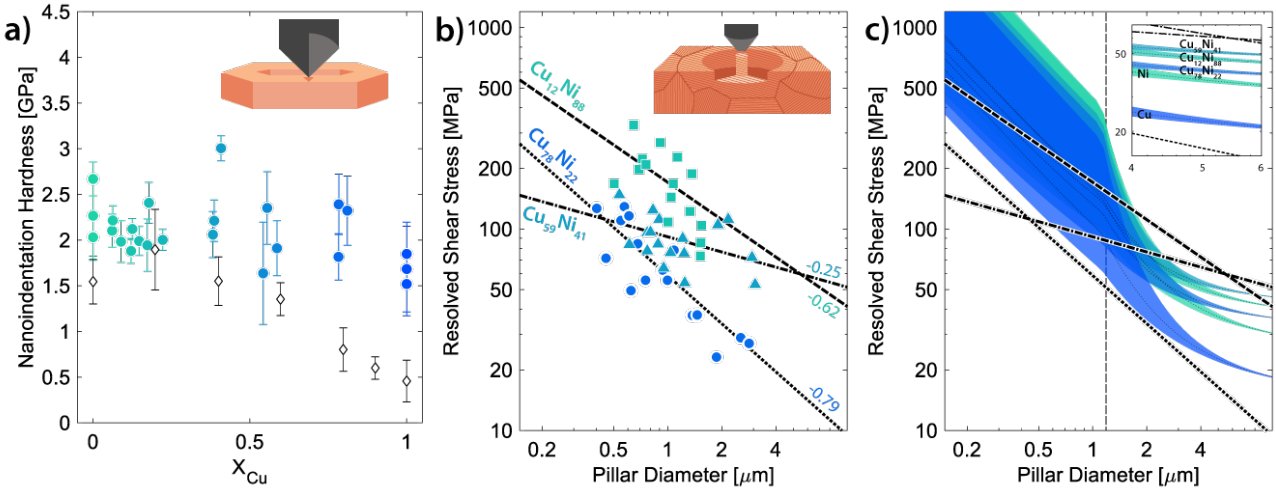

Figure 4. Micromechanical testing of HIAM Cu_xNi. (a) Average nanoindentation hardnesses as a function of composition plotted against literature **[19]**. **(b)** Extrinsic size effects during micropillar compression of FIB-milled single crystals in the absence of boundaries. **(c)** Fit lines from **(b)** plotted against estimated strengths of Cu_xNi solid solutions predicted by a modified stochastic source length model.

To assess the micro- and nanoscale mechanical properties of HIAM-produced Cu_xNi, **Fig. 4** shows their average hardnesses obtained via depth-sensing nanoindentation (**Fig. 4a**) and their critical resolved shear stresses obtained via compression of single crystalline pillars (**Fig. 4b**). In **Fig. 4a** the reported hardnesses span the whole compositional range from pure Ni to pure Cu with each data point representing the average hardness and standard deviation of a unique specimen. Points in black show the hardness reported in literature for diffusion alloyed Cu_xNi solid solutions of similar grain size **[19]**. In comparison to the hardness of Ni and Cu of similar grain size presented in Bahr et al., the average hardness of HIAM Ni and HIAM Cu are at least 0.51 GPa and 0.94 GPa

harder, respectively **[19].** The largest gain in average hardness from literature is 1.15 GPa and 1.37 GPa for HIAM Ni and HIAM Cu respectively. Similar to the pure HIAM Ni and Cu, the HIAM Cu_xNi alloys with $x \geq 40\%$ Cu exceed the reported average hardness. The nominally 80% Cu samples demonstrate the largest increase in hardness of 1.52 GPa (~90% increase). For Ni-rich alloys (nominally 5-20% Cu), the hardness remains consistently around 2.00-2.25 GPa which is comparable to the literature reported hardness of 1.9 ± 0.4 [**19**].

To probe intragranular mechanical behavior in HIAM-fabricated alloys, single crystalline pillars of varying diameters are machined from large grains of as-fabricated polycrystals whose orientations were measured with EBSD. These pillars are visually free from defects like grain boundaries, twin boundaries, and large voids and inclusions. **Fig. 4b** shows the measured shear stress of the representative compositions of Ni-rich ($Cu_{12}Ni_{88}$), equiatomic ($Cu_{59}Ni_{41}$), and Cu-rich ($Cu_{78}Ni_{22}$) alloys. Since each alloy exhibits a size effect characterized by its power law scaling exponent, they display statistically greater shear stress at yielding than reported bulk values **[20-22]**. For the Ni-rich and Cu-rich alloys this exponent lies within the typical range of -0.6 to -0.8 for FCC metals [**23,24**]. However, for near-equiatomic alloys, the exponent of -0.25 is greatly diminished. **Fig. 4c** compares the experimentally determined scaling of yield to the predicted strength of a Cu_xNi solid solution based on a stochastic source length model which attributes size-dependent strengthening to **[25]**.

The vertical line indicates the transition from collective dislocation plasticity to source-controlled plasticity where the power law scaling behavior dominates. The inset highlights the predicted solid solution strengthening behavior in alloys with dimensions of several microns. The model predicts a shift in alloy strength ordering when transitioning to the source-controlled behavior with Cu-rich allows having less strength than pure Ni nanopillars.

Outlook

The integration of nanoscale additive manufacturing with microstructural engineering opens a new design space for hierarchical materials that blend strength, flaw tolerance, and functionality. Future efforts will focus on expanding the material palette, introducing multimaterial architectures, and probing dynamic or cyclic loading conditions to assess durability. These capabilities directly align with DOE priorities in advanced manufacturing, lightweight materials, and resilient infrastructure, and position this platform as a foundational technology for materials innovation at the micro- and nanoscale.

References

[1] Raabe, D., Tasan, C. C. & Olivetti, E. A. Strategies for improving the sustainability of structural metals. *Nature* **575**, 64–74 (2019).

[2] Sames, W. J., List, F. A., Pannala, S., Dehoff, R. R. & Babu, S. S. The metallurgy and processing science of metal additive manufacturing. *International Materials Reviews* **61**, 315–360 (2016).

[3] Herzog, D., Seyda, V., Wycisk, E. & Emmelmann, C. Additive manufacturing of metals. *Acta Materialia* **117**, 371–392 (2016).

[4] Lewandowski, J. J. & Seifi, M. Metal Additive Manufacturing: A Review of Mechanical Properties. *Annual Review of Materials Research* **46**, 151–186 (2016).

[5] Liu, L. *et al.* Dislocation network in additive manufactured steel breaks strength–ductility trade-off. *Materials Today* **21**, 354–361 (2018).

[6] Bertsch, K. M., Meric de Bellefon, G., Kuehl, B. & Thoma, D. J. Origin of dislocation structures in an additively manufactured austenitic stainless steel 316L. *Acta Materialia* **199**, 19–33 (2020).

[7] Li, Z. *et al.* Enhanced strengthening and hardening via self-stabilized dislocation network in additively manufactured metals. *Materials Today* **50**, 79–88 (2021).

[8] Ramirez, D. A. *et al.* Novel precipitate–microstructural architecture developed in the fabrication of solid copper components by additive manufacturing using electron beam melting. *Acta Materialia* **59**, 4088–4099 (2011).

[9] Daryadel, S. *et al.* Localized Pulsed Electrodeposition Process for Three-Dimensional Printing of Nanotwinned Metallic Nanostructures. *Nano Lett.* **18**, 208–214 (2018).

[10] Dehoff, R. R. *et al.* Site specific control of crystallographic grain orientation through electron beam additive manufacturing. *Materials Science and Technology* **31**, 931–938 (2015).

[11] Randle, V. Twinning-related grain boundary engineering. *Acta Materialia* **52**, 4067–4081 (2004).

[12] Watanabe, T. Grain boundary engineering: historical perspective and future prospects. *J Mater Sci* **46**, 4095–4115 (2011).

[13] Saccone, M. A., Gallivan, R. A., Narita, K., Yee, D. W. & Greer, J. R. Additive manufacturing of micro-architected metals via hydrogel infusion. *Nature* **612**, 685–690 (2022).

[14] Zhang, W. *et al.* Suppressed Size Effect in Nanopillars with Hierarchical Microstructures Enabled by Nanoscale Additive Manufacturing. *Nano Lett.* **23**, 8162–8170 (2023).

[15] Yee, D. W. *et al.* Hydrogel-Based Additive Manufacturing of Lithium Cobalt Oxide. *Advanced Materials Technologies* **6**, 2000791 (2021).

[16] Vogl, V., Åhman, M. & Nilsson, L. J. Assessment of hydrogen direct reduction for fossil-free steelmaking. *Journal of Cleaner Production* **203**, 736–745 (2018).

[17] El-Zoka, A. A., Stephenson, L. T., Kim, S.-H., Gault, B. & Raabe, D. The Fate of Water in Hydrogen-Based Iron Oxide Reduction. *Advanced Science* **10**, 2300626 (2023).

[18] Kim, S.-H. *et al.* Influence of microstructure and atomic-scale chemistry on the direct reduction of iron ore with hydrogen at 700°C. *Acta Materialia* **212**, 116933 (2021).

[19] Bahr, D. F. & Vasquez, G. Effect of solid solution impurities on dislocation nucleation during nanoindentation. *Journal of Materials Research* **20**, 1947–1951 (2005).

[20] Kratochvíl, P. & Neradová, E. Solid solution hardening in some copper base alloys. *Czech J Phys* **21**, 1273–1278 (1971).

[21] Osswald, E. Zugversuche an Kupfer-Nickelkristallen. *Z. Physik* **83**, 55–78 (1933).

[22] Suzuki, H. Solution Hardening in Au-Ag and Cu-Ni Alloy Crystals. in Strength of Metals and Alloys (ICSMA 8) (eds. Kettunen, P. O., Lepistö, T. K. & Lehtonen, M. E.) 573–578 (Pergamon, 1989). doi:10.1016/B978-0-08-034804-9.50088-7.

[23] Dimiduk, D. M., Uchic, M. D. & Parthasarathy, T. A. Size-affected single-slip behavior of pure nickel microcrystals. *Acta Materialia* **53**, 4065–4077 (2005).

[24] Jennings, A. T., Burek, M. J. & Greer, J. R. Microstructure versus Size: Mechanical Properties of Electroplated Single Crystalline Cu Nanopillars. *Phys. Rev. Lett.* **104**, 135503 (2010).

[25] Parthasarathy, T. A., Rao, S. I., Dimiduk, D. M., Uchic, M. D. & Trinkle, D. R. Contribution to size effect of yield strength from the stochastics of dislocation source lengths in finite samples. *Scripta Materialia* **56**, 313–316 (2007).

[26] Lisi, N., Dikonimos, T., Buonocore, F. *et al.* Contamination-free graphene by chemical vapor deposition in quartz furnaces. *Sci Rep* **7**, 9927 (2017). https://doi.org/10.1038/s41598-017-09811-z

[27] Maity, P. C., Lahiri, I. & Suresh, K. S. Role of twin boundaries and copper content on the mechanism of recrystallization in Ni-Cu alloys. *Materialia* **22**, 101428 (2022).

[28] Cahoon, J. R., Li, Q. & Richards, N. L. Microstructural and processing factors influencing the formation of annealing twins. *Materials Science and Engineering: A* **526**, 56–61 (2009).

[29] Lu, L., Shen, Y., Chen, X., Qian, L. & Lu, K. Ultrahigh Strength and High Electrical Conductivity in Copper. *Science* **304**, 422–426 (2004).

[30] Hodge, A. M., Wang, Y. M. & Barbee, T. W. Large-scale production of nano-twinned, ultrafine-grained copper. *Materials Science and Engineering: A* **429**, 272–276 (2006).

[31] Mahajan, S., Pande, C. S., Imam, M. A. & Rath, B. B. Formation of annealing twins in f.c.c. crystals. *Acta Materialia* **45**, 2633–2638 (1997).

[32] Gleiter, H. The formation of annealing twins. Acta Metallurgica **17**, 1421–1428 (1969).

[33] Lewis, J. S. The reduction of copper oxide by hydrogen. *J. Chem. Soc.* 820–826 (1932) doi:10.1039/JR9320000820.

[34] Pease, R. N. & Taylor, H. S. THE REDUCTION OF COPPER OXIDE BY HYDROGEN. *J. Am. Chem. Soc.* **43**, 2179–2188 (1921).

[35] Hidayat, T., Rhamdhani, M. A., Jak, E. & Hayes, P. C. On the Relationships between the Kinetics and Mechanisms of Gaseous Hydrogen Reduction of Solid Nickel Oxide. *Metall Mater Trans B* **40**, 474–489 (2009).

[36] Jeangros, Q. *et al.* Reduction of nickel oxide particles by hydrogen studied in an environmental TEM. *J Mater Sci* **48**, 2893–2907 (2013).

[37] Little, J. A., Evans, J. W. & Westmacott, K. H. Early stages of reduction of nickel oxide single crystals: An investigation by transmission electron microscope. *Metall Trans B* **11**, 519–524 (1980).

[38] Pöyhtäri, S. et al. Kinetic Analysis of Hydrogen Reduction of Nickel Compounds. Metall Mater Trans B (2023) doi:10.1007/s11663-023-02955-6.

[39] Zou, L., Li, J., Zakharov, D., Stach, E. A. & Zhou, G. In situ atomic-scale imaging of the metal/oxide interfacial transformation. Nat Commun **8**, 307 (2017).

[40] Rodriguez, J. A., Kim, J. Y., Hanson, J. C., Pérez, M. & Frenkel, A. I. Reduction of CuO in H2: In Situ Time-Resolved XRD Studies. Catalysis Letters **85**, 247–254 (2003).

[41] Rodriguez, J. A., Hanson, J. C., Frenkel, A. I., Kim, J. Y. & Pérez, M. Experimental and Theoretical Studies on the Reaction of H2 with NiO: Role of O Vacancies and Mechanism for Oxide Reduction. J. Am. Chem. Soc. **124**, 346–354 (2002).

[42] Zhang, R. *et al.* Short-range order and its impact on the CrCoNi medium-entropy alloy. *Nature* **581**, 283–287 (2020).

[43] Chen, X. *et al.* Direct observation of chemical short-range order in a medium-entropy alloy. *Nature* **592**, 712–716 (2021).

[44] Coury, F. G., Miller, C., Field, R. & Kaufman, M. On the origin of diffuse intensities in fcc electron diffraction patterns. *Nature* **622**, 742–747 (2023).

[45] Xiao, H. Z. & Daykin, A. C. Extra diffractions caused by stacking faults in cubic crystals. *Ultramicroscopy* **53**, 325–331 (1994).

[46] Clapp, P. C. Atomic Configurations in Binary Alloys. *Phys. Rev. B* **4**, 255–270 (1971).

[47] Mozer, B., Keating, D. T. & Moss, S. C. Neutron Measurement of Clustering in the Alloy CuNi. *Phys. Rev.* **175**, 868–876 (1968).

[48] Turchanin M.A., Agraval P.G., and Abdulov A.R. Phase equilibria and thermodynamics of binary copper systems with 3d-metals. VI. Copper-nickel system, *Powder Metall. Met. Ceram.* **46**, 467-477 (2007).

[49] Lu, L. *et al.* Nano-sized twins induce high rate sensitivity of flow stress in pure copper. *Acta Materialia* **53**, 2169–2179 (2005).

[50] Labusch, R. A Statistical Theory of Solid Solution Hardening. *physica status solidi (b)* **41**, 659–669 (1970).

[51] Fleisgher, R. L. Solution hardening. *Acta Metallurgica* **9**, 996–1000 (1961).

[52] Suzuki, T., Takeuchi, S. & Yoshinaga, H. Dislocation Motion in the Field of a Random Distribution of Point Obstacles: Solution Hardening. in *Dislocation Dynamics and Plasticity* (eds. Suzuki, T., Takeuchi, S. & Yoshinaga, H.) 32–46 (Springer, 1991). doi:10.1007/978-3-642-75774-7_3.

[53] Nakanishi, Kyôji, and Hideji Suzuki, 'Analysis of the Grain Size Dependence of the Yield Stress in Copper-Aluminum and Copper-Nickel Alloys', *Transactions of the Japan Institute of Metals*, 15.6 (1974), 435–40 <https://doi.org/10.2320/matertrans1960.15.435>

[54] El-Awady, J. A. *et al.* Pre-straining effects on the power-law scaling of size-dependent strengthening in Ni single crystals. *Scripta Materialia* **68**, 207–210 (2013).

[55] Schneider, A. S. *et al.* Influence of bulk pre-straining on the size effect in nickel compression pillars. *Materials Science and Engineering: A* **559**, 147–158 (2013).

[56] Gu, R. & Ngan, A. H. W. Size effect on the deformation behavior of duralumin micropillars. *Scripta Materialia* **68**, 861–864 (2013).

[57] Girault, B., Schneider, A. S., Frick, C. P. & Arzt, E. Strength Effects in Micropillars of a Dispersion Strengthened Superalloy. *Advanced Engineering Materials* **12**, 385–388 (2010).

[58] Li, S.-H., Zhao, Y., Lau, K. B., Wang, P. & Upadrasta, R. Micropillar compression investigation on the mechanical behavior of Ni manufactured using laser powder bed fusion. *Materials Science and Engineering: A* **879**, 145269 (2023).

[59] Greer, J. R., Oliver, W. C. & Nix, W. D. Size dependence of mechanical properties of gold at the micron scale in the absence of strain gradients. *Acta Materialia* **53**, 1821–1830 (2005).